

Article

Flow Characteristic Analysis of the Impeller Inlet Diameter in a Double-Suction Pump

Hyunjun Jang ^{1,2}  and Junho Suh ^{1,*} 

¹ Department of Mechanical Engineering, Pusan National University, Busan 43241, Republic of Korea; hyunjun9559@gmail.com

² High Turbo Machinery (HTM) Co., 2, Busandaehak-ro, 63 beon-gil, Geumjeong-gu, Busan 46241, Republic of Korea

* Correspondence: junhosuh@pusan.ac.kr

Abstract: Pumps are considered crucial mechanical devices in any industry. Especially, double-suction pumps, due to their high-flow design and high head, are utilized in diverse industrial sectors. However, despite these advantages, double-suction pumps are vulnerable to issues like losses, vibrations, and cavitation. Pump vibration is mainly caused by suction recirculation occurring at the impeller inlet. Therefore, this study investigates the impact of the impeller inlet design on enhancing the stability of double-suction pumps while expanding the operating flow range. Through a validated CFD study, the influence of the impeller inlet passage size on the head and efficiency was analyzed. Furthermore, research was conducted on the phenomenon of suction recirculation occurring at the impeller inlet, proposing design guidelines to minimize it, especially for operation at low flow rates. The results demonstrate that the ratio of the hub diameter to the shroud diameter at the impeller inlet significantly impacts the avoidance of recirculation at low flow rates. These findings are expected to contribute to improving the stability and efficiency of high-flow pumps.

Keywords: double-suction pump; suction recirculation; impeller eye diameter; pump; CFD



Citation: Jang, H.; Suh, J. Flow Characteristic Analysis of the Impeller Inlet Diameter in a Double-Suction Pump. *Energies* **2024**, *17*, 1989. <https://doi.org/10.3390/en17091989>

Academic Editor: Pietro Zunino

Received: 15 February 2024

Revised: 27 March 2024

Accepted: 3 April 2024

Published: 23 April 2024



Copyright: © 2024 by the authors. Licensee MDPI, Basel, Switzerland. This article is an open access article distributed under the terms and conditions of the Creative Commons Attribution (CC BY) license (<https://creativecommons.org/licenses/by/4.0/>).

1. Introduction

Pumps are widely used in various industries, including building management, manufacturing, and petrochemical plants. Among these pumps, the double-suction pump is highly valued due to its special characteristics and performance. A double-suction pump is a type of centrifugal pump that has been utilized in various forms and applications for centuries. The double-suction pump is particularly recognized for its high capacity. Its distinguishing features are the suction inlets that are located on both sides of the impeller. This design allows double-suction pumps to operate with high efficiency and expand its range of applications. Therefore, they are widely used in various industries. Additionally, double-suction pumps can implement a high flow rate and be used in high-head systems. Moreover, due to their structural and flow characteristics, the suction of equal amounts of fluid on both sides of the impeller generates less axial force compared to single-suction pumps. However, these pumps may be susceptible to issues such as losses due to complex fluid pathways, vibrations, and cavitation. Various studies are underway to address these issues, and papers and patents related to this topic continue to be published. According to the vibration standards of API610 [1] provided by the American Petroleum Institute, the operating range of pumps is divided into a Preferred Operating Region (POR) and Allowable Operating Region (AOR). Typically, the flow range of the POR is 70% to 120% of the pump's flow rate at the Best Efficiency Point (BEP). Furthermore, API610 claims the vibration of an overhung (OH)-type, single-stage pump and a between-bearing (BB)-type, double-stage pump should not exceed 3.0 mm/s. The AOR vibration standard is +30% of the POR standard, not exceeding 3.9 mm/s. The operating range of a pump refers to the flow range that does not exceed the vibration limit of the AOR, with the minimum

flow point represented as the pump's minimum flow rate. Vibrations are often significant under part-load conditions, related to the fluid's vortex characteristics [2]. Frequency analysis shows that these phenomena occur very broadly below 1X of the Vane-Passing Frequency (VPF). Such sources of vibration, caused by recirculation, vortices, stall, pressure fluctuation, etc., need to be improved for the fatigue life of the pump and for noise and vibration reduction [3].

Fraser et al. observed that suction recirculation in centrifugal pumps causes surges, high noise decibels, and abnormal vibrations [4]. Experimental evidence showed cavitation-induced erosion despite an adequate Net Positive Suction Head (NPSH). Breugelmans and Sen experimentally observed recirculation at impeller inlets with varying shapes [5]. Ashihara and Goto used steady-state CFD analysis to study suction recirculation in inducers, comparing the alignment with experimental results [6]. Using the CFD flow behavior, the presence of vibrations can be predicted in the pumps [2,7], rather than estimating their intensities. Fluid-induced instability is the main cause of pump vibrations, which are indicated as flow circulations, vortices, and pressure fluctuations [8,9] as they can visualize in detail using CFD simulations [2,7]. Therefore, one of the aims of this CFD study is to determine the vibration condition based on the flow recirculation phenomenon occurring at the impeller inlet of a pump.

Yamanishi et al. [10] and Kang et al. [11] researched the flow instability in inducers due to inlet recirculation using CFD simulations with an LES turbulence model. Shim et al. [12] analyzed various impeller designs to reduce suction recirculation and cavitation using CFD simulation with the shear stress transport (SST) turbulence model and multi-objective optimization. The pump studies discussed above were conducted to observe and mitigate recirculation in OH-type, single-suction pumps. Furthermore, studies on double-suction pumps have also been carried out by many researchers. Capurso, T. [13] investigated performance variations based on the impeller geometry of double-suction pumps using OpenFOAM simulation, comparing it with experimental measurements. Yao [14] conducted an experiment with pulsation measurements of the casing and the impeller of a double-suction pump, and the pressure fluctuations of a double-suction centrifugal pump were experimentally investigated by Wang [15] to determine the effects of the flow rate and rotation speed. Hatano [16] used CFD simulation alone with a $k-\epsilon$ turbulence model and an experimental study to observe the cavitation stability of a double-suction centrifugal pump. The impact of the outer diameter of the impeller exit on the pump performance and cavitation was studied by Matlakala, M.E. [17] using affinity laws, and its safety was analyzed through structural analysis. Al-Obaidi, A. [18] conducted CFD simulation with an SST turbulence model to detect cavitation's occurrence at various outlet impeller diameters and flow rates and make correlations. W. Shi [19] examined performance changes based on the shape of the impeller exit using CFD simulations, while Reddy S.T.C [20] hypothesized the optimal value for the diffuser outlet width using experimental methods. Tan Ming-Gao [21] found that the blade outlet width of a centrifugal pump had a clear effect on the design point characteristics, flow field, and performance curve shape via CFD simulations. There are numerous preliminary studies investigating the recirculation phenomenon at the impeller inlet and pump cavitation. D. Zhu [22], Sano [23], Balasubramanian [24], and Dönmez, A. H. [25] mainly researched cavitation based on the leading edge shape of the impeller inlet using CFD and experimental methods. Luo [26] conducted research on the effects of the starting point and the size of the impeller's leading edge, and Shukla [27] carried out both experimental and numerical studies on the cavitation performance related to variations in the inlet diameter. Researchers studying turbo-machinery have conducted various studies on fluid instability [28,29] and vortices [30], and research on optimization methods is also being conducted [31,32].

Even though there have been many studies on pumps, impeller geometry, and impeller-related cavitation and performance enhancement, only a few studies have been conducted to analyze the vibration phenomenon in double-suction pumps. Thus, the effect of the size of the impeller inlet passage on flow-circulation-related vibration has not been pre-

viously researched. Therefore, this study analyzed the flow characteristics, mainly the recirculation phenomenon, of double-suction pumps based on the impeller's inlet width using experimental and numerical methods to confirm the performance at various flow rates. The impeller width was varied based on the ratio of the hub diameter to the shroud diameter. It examined the recirculation phenomena and their magnitudes and locations of formation depending on the five different inlet widths. This led to predictions of the flow points where recirculation would occur based on the ratio of the hub diameter to the shroud diameter at the impeller inlet, deriving design strategies to minimize it.

The manuscript starts with a brief introduction of double-suction pumps, explaining their advantages and applications and previous studies on improvements, followed by identifying the research gap. Section 2 describes the pump geometry and the design procedure, especially the design criteria for the impeller eye diameter. Numerical validation is discussed in Section 3 by comparing the results with experiments conducted for the available pump design. The core interest of this research is explained in Section 4, discussing the flow characteristics of five impeller inlet designs, identifying the circulation occurrence at the flow points, and leading to findings on the appropriate impeller hub-to-shroud-diameter ratio for an optimal design. The manuscript concludes by summarizing the research findings, mentioning their importance to industrial applications.

2. Pump Design

2.1. Geometry

The design of pumps is a complex process that requires consideration of various factors. In particular, the operating conditions, fluid characteristics, and the size of the pump have a decisive impact on its performance and efficiency. These factors must be carefully considered during the design process. While double-suction pumps demonstrate excellent performance in supplying high flow rates, they tend to be susceptible to cavitation. Cavitation is a phenomenon in which liquid forms into vapor due to low pressure within the pump, leading to performance degradation and damage. The inlet diameter of the impeller is a particularly important design factor, determined by the capacity and speed of the pump. This significantly affects the pump's performance, and therefore the selection of an appropriate inlet diameter greatly influences the overall performance of the pump.

The flow passage shape of a double-suction pump is as depicted in Figure 1. This design is from an actual pump manufacturer with field operation experience. The pump, known to have noise and vibration issues, was used as a reference for this study.

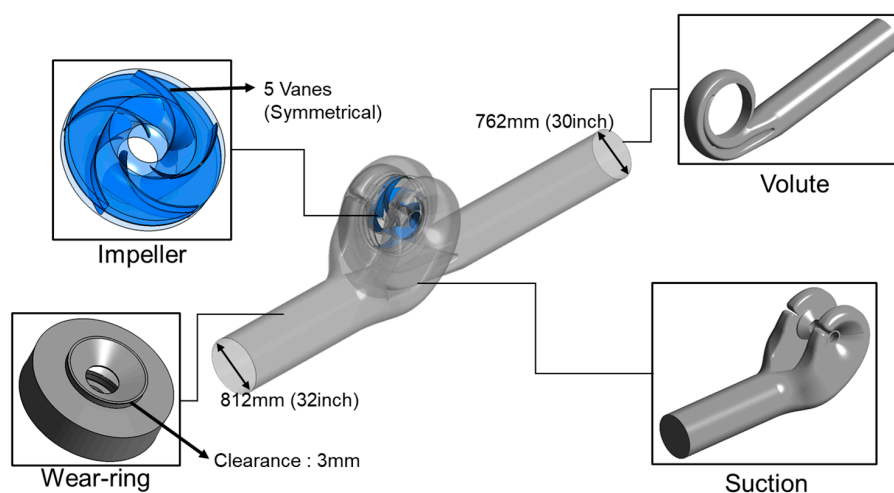


Figure 1. Three-dimensional modeling.

The suction pump has an inlet diameter of approximately 812 mm (32 inches), and the fluid enters through the suction inlet, divided between both sides before flowing into the impeller's inlet. The impeller has five vanes on the same plane at equal spacing with a

symmetrical arrangement. The volute passage in double-suction pumps has splitters inside to mitigate radial thrust in high-flow and high-head conditions. High radial thrust can lead to rapid wear-ring wear and potential shaft fatigue. Therefore, the design includes a double structure with splitters. The volute outlet diameter is 762 mm (30 inches). The wear-ring, between the rotating and non-rotating parts, is designed with a gap, having a unilateral clearance of 3.0 mm, and its shape is taken into consideration. The horizontal length of the modeling from the inlet to the outlet of the pump is approximately 7.28 m.

2.2. Design of the Impeller Inlet

In designing impellers to counteract cavitation, it is imperative to achieve a low NPSH_{re} (Net Positive Suction Head required). One strategy involves increasing the inlet area of the impeller's design, often entailing the enlargement of the impeller's eye diameter based on the designer's experience. Gulich [33] suggests that for centrifugal pumps, the eye diameter should adhere to the equation specified in Equation (1). This research has also adopted this equation as a foundation, progressing beyond experience-based designs aimed at avoiding cavitation towards formulating designs that effectively suppress recirculation.

$$d_{1a} = 2.9 \sqrt[3]{\frac{Q_{La}}{f_q n k_n \tan \beta_1} \left(1 + \frac{\tan \beta_1}{\tan \alpha_1}\right)} \quad (1)$$

Q_{La} : Flow rate through impeller: $Q_{La} = Q + Q_{sp} + Q_E + Q_h = Q/\eta_v$

- Q : Flow rate, volumetric flow
- Q_{sp} : Leakage flow rate through the seal at the impeller inlet
- Q_E : Flow rate through axial-thrust-balancing device
- Q_h : Flow rate through auxiliaries (mostly zero)
- η_v : Volumetric efficiency

f_q : Impeller eyes per impeller: single-entry $f_q = 1$; double-entry $f_q = 2$

n : Rotational speed (revolutions per minute)

k_n : Blockage caused by hub: $k_n = 1 - d_n^2/d_1^2$

d_n : Hub diameter

α_1 : Angle between directions of circumferential and absolute velocity, 1: impeller blade's leading edge

β_1 : Angle between relative velocity vector and the negative direction of circumferential velocity, 1: impeller blade's leading edge

Figure 2 represents one of the impeller inlet passages. The horizontal red line denotes the z-axis, while the vertical red line signifies the R-axis. The term d_{1a} refers to the shroud diameter, and d_{1i} indicates the hub diameter of the impeller inlet [33]. Referring to the illustration in Figure 2, the impeller inlet's width was set to five different sizes, as detailed in Table 1.

Table 1. Impeller eye diameters of cases.

	d_{1a} Decrease Ratio	d_{1a} [mm]	d_{1i} [mm]	d_{1a}/d_{1i}
Case 1	1.00	586.0		2.20
Case 2	0.97	566.0		2.12
Case 3	0.94	548.0	266.6	2.06
Case 4	0.91	534.0		2.00
Case 5	0.88	514.0		1.93

The distance between the impeller's hub and the shroud were set to five different sizes, as shown in Table 1, while altering only the outer diameter of the shroud with a constant hub diameter. The hub diameter at the impeller inlet is 266.6 mm. The shroud diameter in Case 1 was 586.0 mm. From Case 1 to Case 5, the diameter was reduced by 3% incrementally. The shroud diameter in Case 4 is the size calculated using Equation (1).

The shape of Case 1 is designed to be 9% larger than the size of Case 4, and Case 5 is about 3% smaller.

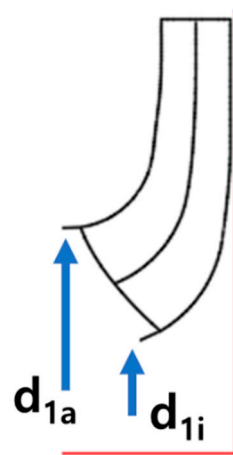


Figure 2. Hub and shroud diameter location at impeller inlet [33].

Generally, the impeller's outlet affects the pump's head [17–21]. Among the conventional design methods, the theoretical formula for the impeller exit follows Equation (2), and the design was conducted by referring to this equation. In this paper, the outer diameter (d_2) and width (b_2) of the impeller's outlet, as well as the exit blade angle, were kept constant across all cases. The impeller inlet has the most influence on the stability of the pump and cavitation [22–27]. Therefore, this study fixed the diameter of the impeller's hub (d_{1i}) and varied the shroud size (d_{1a}) at the inlet as described earlier, aiming to understand how the ratio of the diameter of the hub to the diameter of the shroud at the impeller inlet affects the pump's performance and stability.

$$d_2 = \frac{60 \times u_2}{\pi \times n} \quad (2)$$

d_2 : Impeller's outer diameter

u_2 : Impeller's outer diameter tip speed, $u_2 = K_u \sqrt{2gH}$

- K_u : The values computed using a Stepanoff chart. [34]
- H : Head, $H = \frac{P_{Total, outlet} - P_{Total, Inlet}}{\rho g}$ (m)
- g : Gravitational acceleration (m/s^2)
- ρ : Liquid density (kg/m^3)

3. Numerical and Experimental Methods

3.1. Experimental Method

To ensure the reliability of the flow analysis, a pump performance experiment was conducted on Case 1 among the five impeller configurations. Figure 3 displays the assembled pump manufactured for the experiment. To verify the pump's performance, the measurements included the flow rate (Q [m^3/h]), total head (H [m]), liquid temperature (T [$^{\circ}C$]), and power (P).

Flow measurements were taken at pump discharge using an electronic flow meter (KTM-800, Korea Flowmeter Co. LTD, Incheon, Republic of Korea) with a maximum measuring range of $18,000 m^3/h$ and a maximum error of 0.5%, as verified using technical data. For the total head measurement, the pressure was taken at a position three times the diameter away from the pump's suction casing inlet, and the discharge pressure was measured five diameters away from the discharge volute outlet. A pressure transmitter (266GST, ABB Asea Brown Boveri Ltd, Zurich, Switzerland) was used for the pressure measurements, with a maximum range of 30 bar and a maximum error of 0.04%, as stated in

the technical documentation. The liquid temperature was measured at the pump's suction inlet. The pump's performance was evaluated at a total of 7 flow rates, including the check point, based on the flow rate.

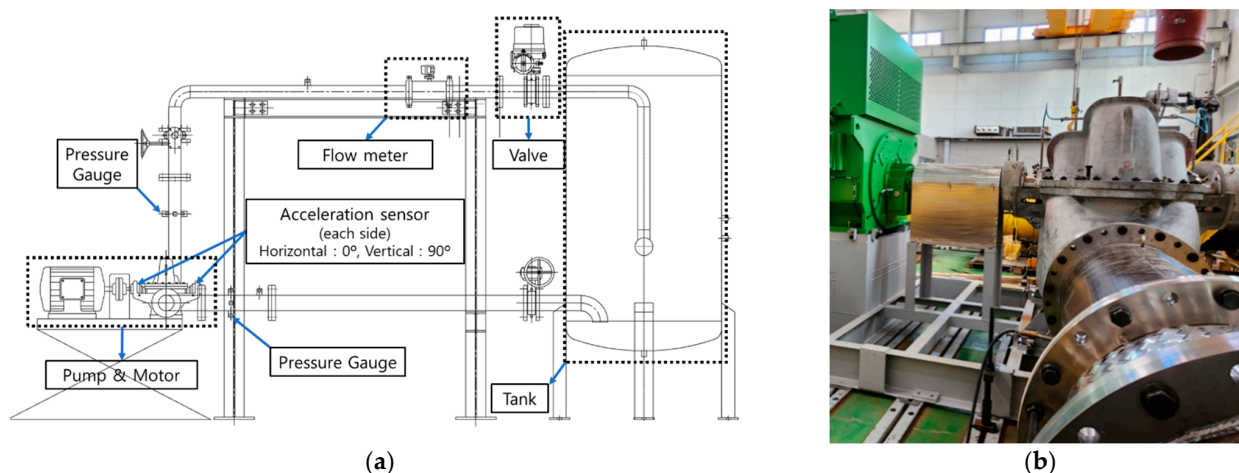


Figure 3. Experimental setup of evaluating the pump performance: (a) schematic diagram, (b) laboratory testing model.

3.2. Flow Analysis Verification with a Numerical Method

The CFD analysis was conducted using ANSYS CFX ver. 2021 R2 under steady-state conditions. ANSYS Mesh was utilized for the grid generation with a Tetra-Prism mesh for the suction and volute, while ICEM CFD was used with a Hexahedral mesh for the wear-ring, which has a thin clearance shape in the impeller. For the impeller, a Hexahedral mesh was created for one of ten blades using TurboGrid, considering all the impellers using replication and symmetry during the analysis.

Before verifying the pump's performance, it was essential to determine an appropriate number of nodes to ensure grid dependency did not affect the results. The properties were based on water at 25 °C, with a density of 997.0 kg/m³. No heat transfer analysis was conducted. The boundary conditions were set with a reference pressure of 1.0 atm, the inlet at 0 Pa, and the outlet at the mass flow rate [kg/s], corresponding to 7500 m³/h. The impeller's rotation speed was 710 rpm. A shear stress transport (SST) turbulence model was used as the turbulence numeric in the RANS model since it captures the flow behavior inside and outside the boundary layer with a combination of $k-\epsilon$ and $k-\omega$ models [35,36]. Furthermore, the SST model simulates the induced flows and vortices in rotating machines much more accurately compared to other turbulence models [37–41]. A high-resolution advection scheme and a turbulence numeric were used in the CFX solver settings, and the energy equation was not activated since the simulation solves for an incompressible flow without a heat transfer model. The impeller inlet interface option was set as Frozen rotor and the exit as Stage according to the CFX documentation. Table 2 summarizes the CFX solver settings, indicating the boundary conditions.

Table 2. CFX solver settings.

Material	Water 25 [°C] (997.0 [kg/m ³])
Heat Transfer	None
Reference Pressure	1.0 [atm]
Turbulence	Shear Stress Transport (SST)
Rotation Speed	710 [rpm]
Inlet	0 [Pa]
Outlet	Mass flow rate [kg/s]
Walls	No Slip

Assuming that an increased mesh number reduces spatial errors, the node count was varied to observe the results. Mesh refinement was carried out while maintaining the average y^+ value at less than 10. To better predict the boundary-layer flow, more than 10 rows of Prism grid layers on the wall were used. With 12,691,000 nodes, an increase of approximately 10% in the mesh led to a 0.5% change in the head as illustrated in Figure 4. A decrease of about 10% in the node count resulted in a 2% change in the head. Therefore, the flow analysis was conducted with the fourth-largest node count resolution, where the head value showed a negligible change with the node count.

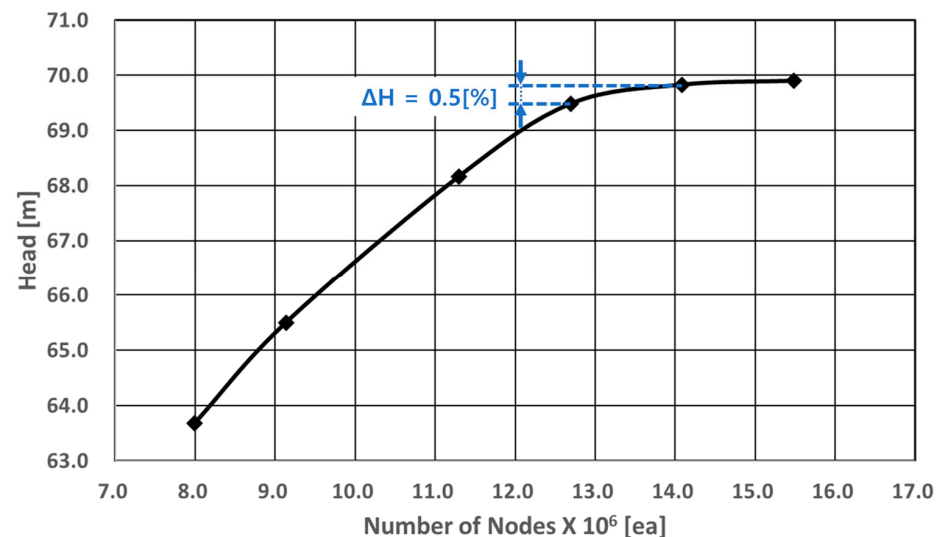


Figure 4. Change in head depending on the number of nodes.

Table 3 organizes the node counts used for each part of the analysis, specifying that the node count for the impeller accounts for ten blades. The impeller represents approximately 52% of the entire mesh. The total node count utilized for the flow analysis was 12,691,000 [EA]. Additionally, Figure 5 displays the mesh configuration of the impeller.

Figure 6 compares the experimental results with the CFD outcomes for a double-suction pump equipped with Case 1's impeller. The CFD analysis was performed at seven flow points ranging from 0.6 to 1.2, including the flow at the BEP (Best Efficiency Point), increasing the flow by 10% each time.

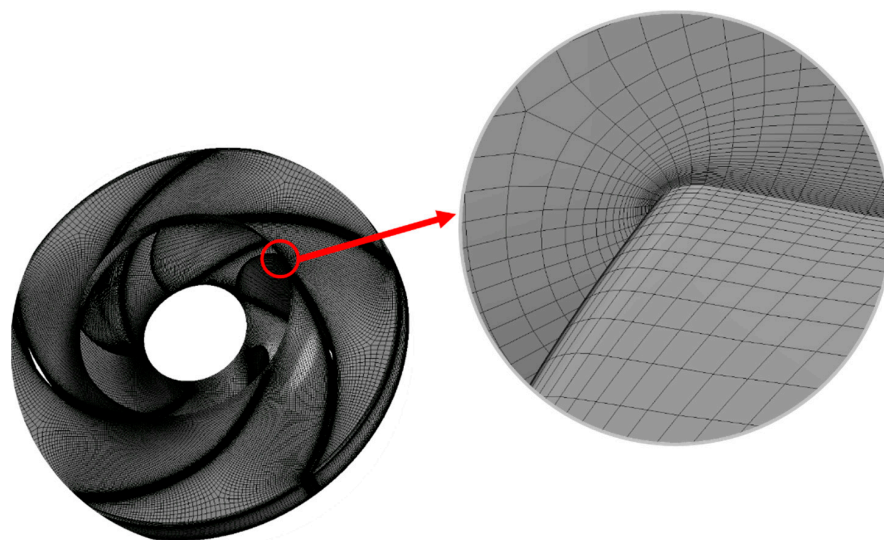
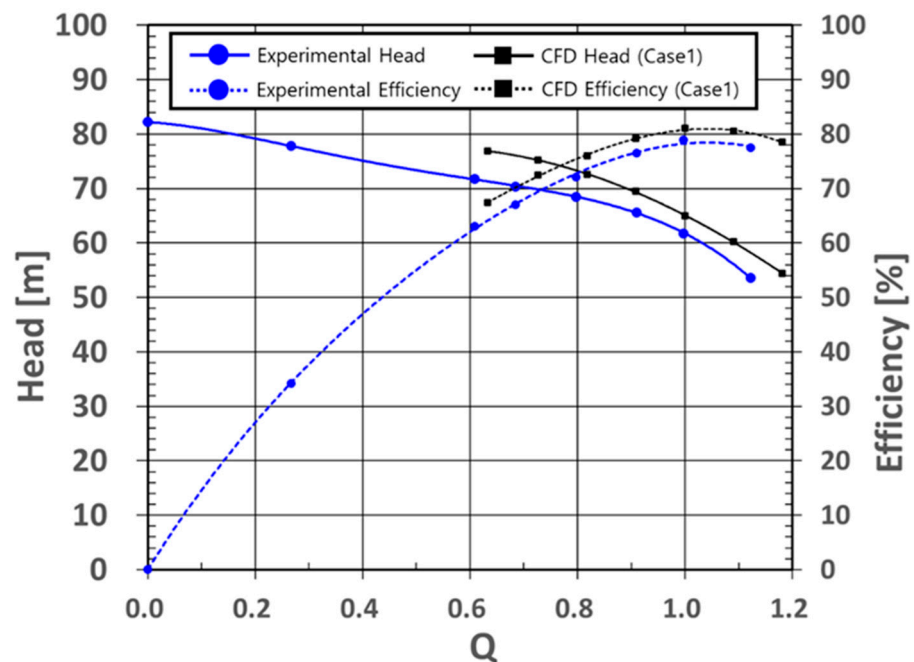


Figure 5. Shape of impeller mesh.

Table 3. Mesh type and number of nodes.

Part	Mesh Type	Number of Nodes
Suction	Tetra-Prism	2,720,313
Impeller (10ea)	Hexahedral	6,641,940
Wear-ring	Hexahedral	2,880,960
Volute	Tetra-Prism	447,787
Total	-	12,691,000

**Figure 6.** Comparison of CFD and experimental results.

The horizontal axis Q in Figure 6 represents the flow point, which means the ratio of the measured flow rate to the flow rate at the highest efficiency. The flow point is 1.0 when the flow rate is $8250 \text{ m}^3/\text{h}$. At the pump's main operating flow point, 0.9 ($7500 \text{ m}^3/\text{h}$), the CFD analysis predicted a 6.1% higher head and a 3.7% higher efficiency compared with the experiment. The highest efficiency point, both in the experimental and CFD results, was recorded at flow point 1.0, but a 5.4% higher head and a 2.6% higher efficiency were predicted in the CFD analysis than the experiment. The minimum discrepancy between the experiment and CFD analysis occurred at the BEP. At the 0.6 flow point, approximately 40% lower than the BEP, the CFD analysis predicted a 7.8% higher head and a 4.5% higher efficiency. It is observed that at the BEP, where secondary flows are minimal, the difference between the CFD simulation and the experiment is relatively small. As one moves away from the BEP, towards lower or higher flows, irregular secondary flows increase, leading to greater losses, reduced efficiency, and larger discrepancies between the CFD and experimental results.

4. Results

4.1. Performance Analysis

To observe the changes in the head and efficiency as pump performance indicators, the flow rate was varied, and the performance was measured at each rate. The flow rate $Q:1.0$ is $8250 \text{ m}^3/\text{h}$. The performance difference was examined by incrementally increasing Q from 0.6 to 1.2 by 10%.

Figure 7a compares the changes in the head with varying flow rates. A notable head difference is observed at lower flow rates when the impeller inlet's width varies. Comparing

the head at flow point 0.6, the largest diameter (Case 1) and the smallest diameter (Case 5) differ by 4.26%. The difference in the head diminishes with an increasing flow, indicating that the size of the impeller inlet significantly impacts its low-flow performance. Larger impeller inlets, or greater differences in diameter between the hub and shroud, lead to a higher head at lower flows, suggesting an effect on the slope of the pump's head curve.

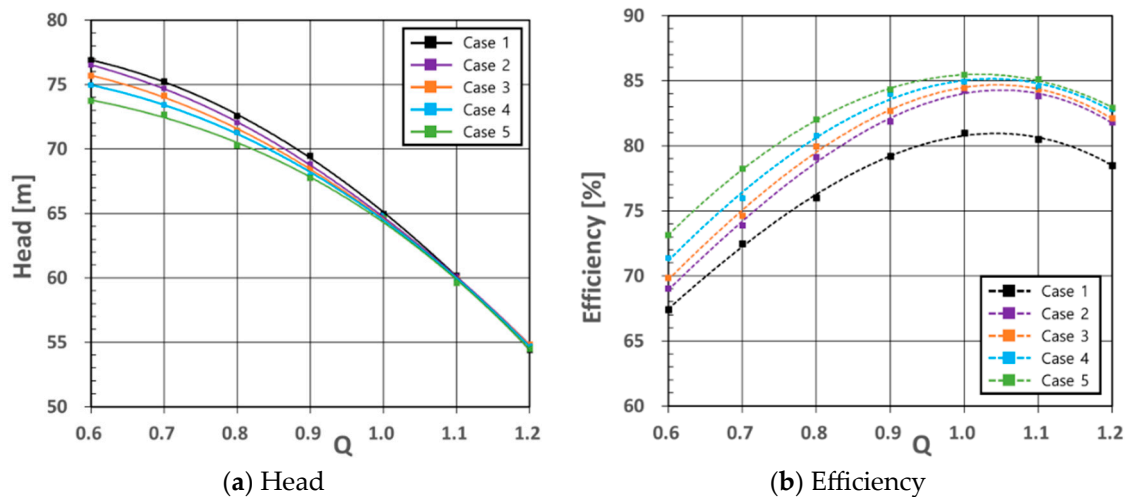


Figure 7. Performance comparison by impeller eye diameter.

Figure 7b shows a comparison of efficiency. As the impeller inlet's diameter decreases, its efficiency increases across all flow rates, especially at lower flows, with the difference diminishing at higher flows. The largest inlet impeller size (Case 1) shows a significantly lower efficiency compared to the other cases, implying higher torque and thus more work on the part of the impeller, leading to greater losses. The head and efficiency are highly affected at lower flows, whereas they show less of a difference at higher flows. A too-large difference in diameter between the hub and shroud, as in Case 1, results in a significantly lower efficiency.

The torque of a pump can be explained by understanding the relationship between the head and efficiency variation. As the pump torque increases, the head relatively increases, but the efficiency tends to decrease. This happens because as the torque increases, the required energy consumption also increases. The results of Figure 7 show that when the impeller eye diameter is large, the head is high at low flow rates, while the efficiency is low. This implies that an impeller with a large eye diameter requires more torque due to the recirculation phenomenon that occurs at the impeller's intake.

4.2. Suction Recirculation Analysis

Figure 8 shows the velocity streamline for different flow points in Case 1, the largest impeller inlet. The recirculation at the impeller inlet can clearly be observed using streamlines. Recirculation, signifying backward flow, starts to appear below the 1.0 flow point, identifying the typical phenomenon occurring at low flow rates, not near the BEP. However, circulation is also observed in Case 1 at the BEP, where the flow point is 1.0. As the flow rate decreases, the backward flow characteristic intensifying at the pump inlet becomes more pronounced. This reverse flow re-enters the impeller, leading to an increased workload and reduced efficiency. The reverse flow also impacts the suction casing, connected to the pump's bearing housing, directly influencing the vibrational effect. In the experiment of Case 1, vibration was recorded as 3.0 mm/sec at the 1.0 flow point, whereas it was increased at lower flow rates. This high vibration characteristic is attributed to the suction recirculation impacting the suction casing.

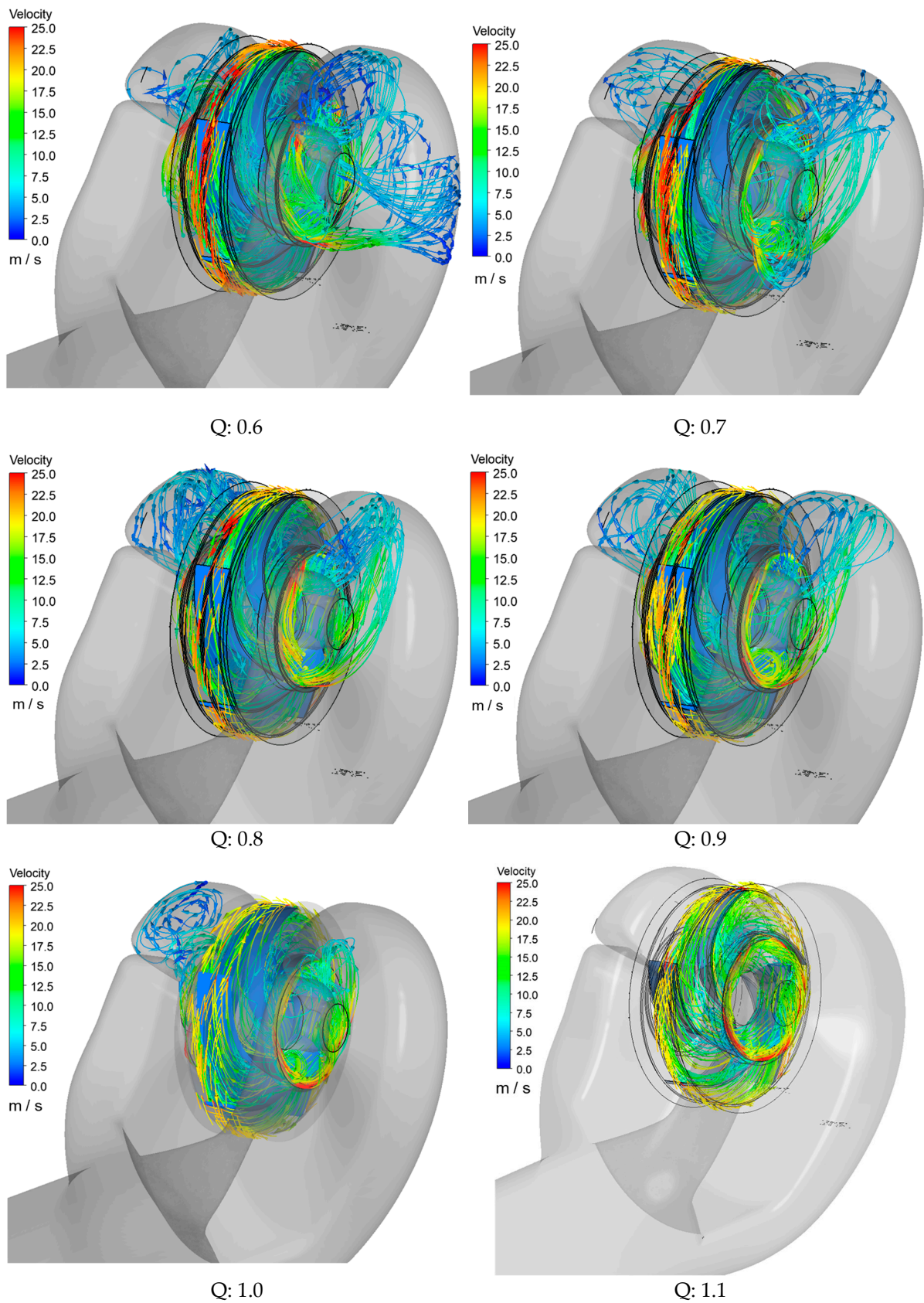


Figure 8. Suction recirculation expressed as a streamline in Case 1.

Figure 9 displays the velocity distribution in the streamwise direction from the meridional plane for Case 1. The analysis using ANSYS CFD-Post Turbo Mode highlights the negative velocities, indicating a flow opposite to the impeller's discharge direction. Lower flow rates exhibit stronger backward flows, particularly near the impeller's shroud. These negative velocities are less pronounced near the hub, indicating a positive flow towards the impeller discharge. This trend suggests that at lower flow rates, the main flow is directed more towards the hub.

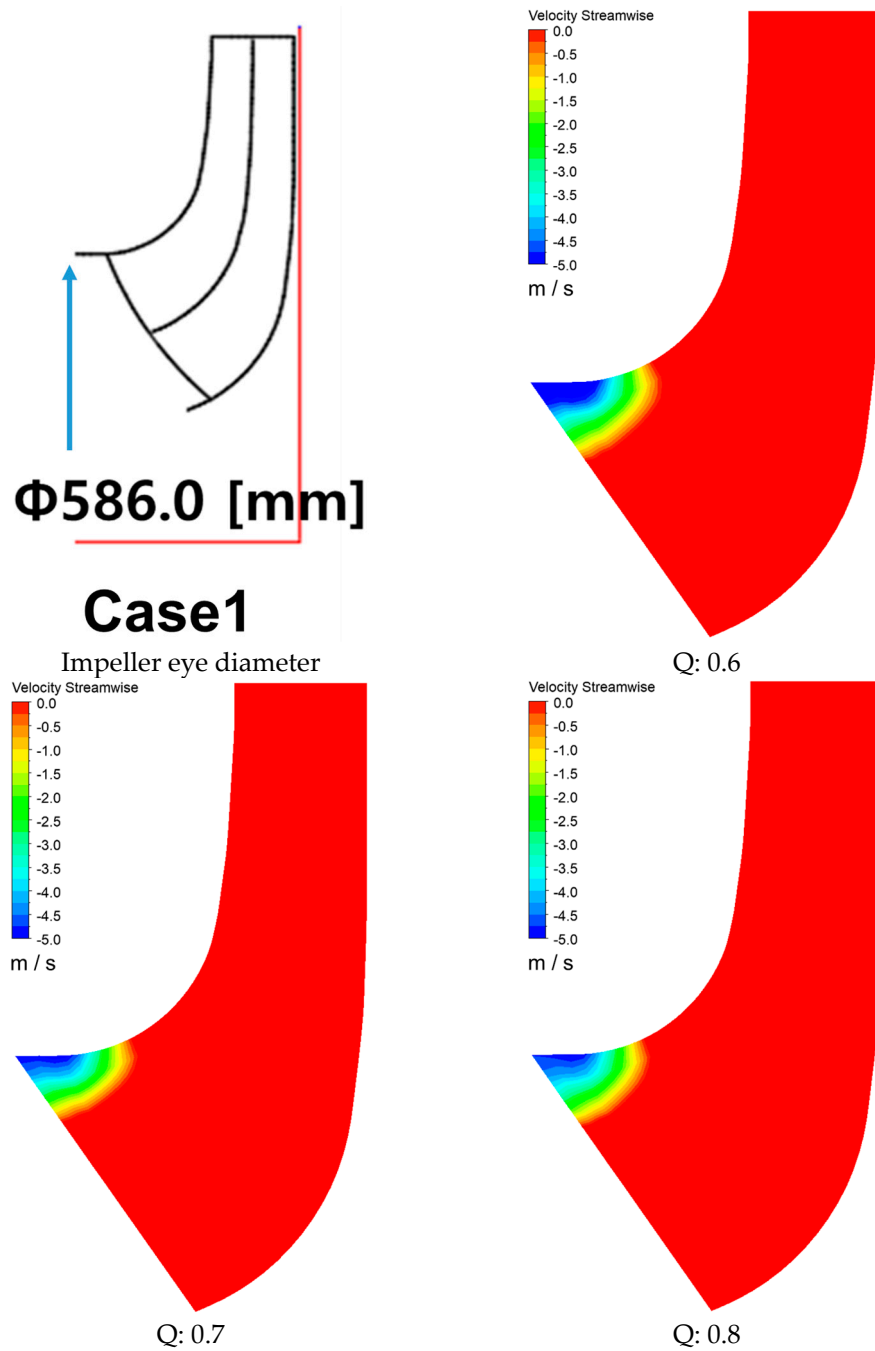


Figure 9. Cont.

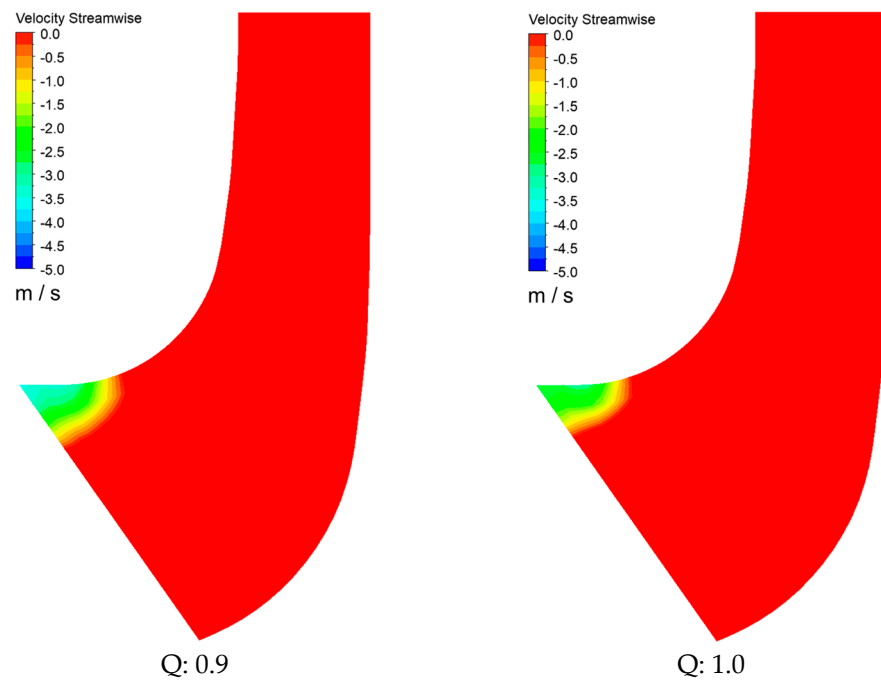


Figure 9. Velocity in the streamwise direction from the meridional plane (Case 1).

Figure 10 examines the suction recirculation in Cases 2 to 5 through streamlines, identifying the flow rates at which recirculation occurs or does not. The analysis qualitatively shows that decreasing the impeller shroud’s diameter by 3% progressively reduces the flow rate where suction recirculation starts.

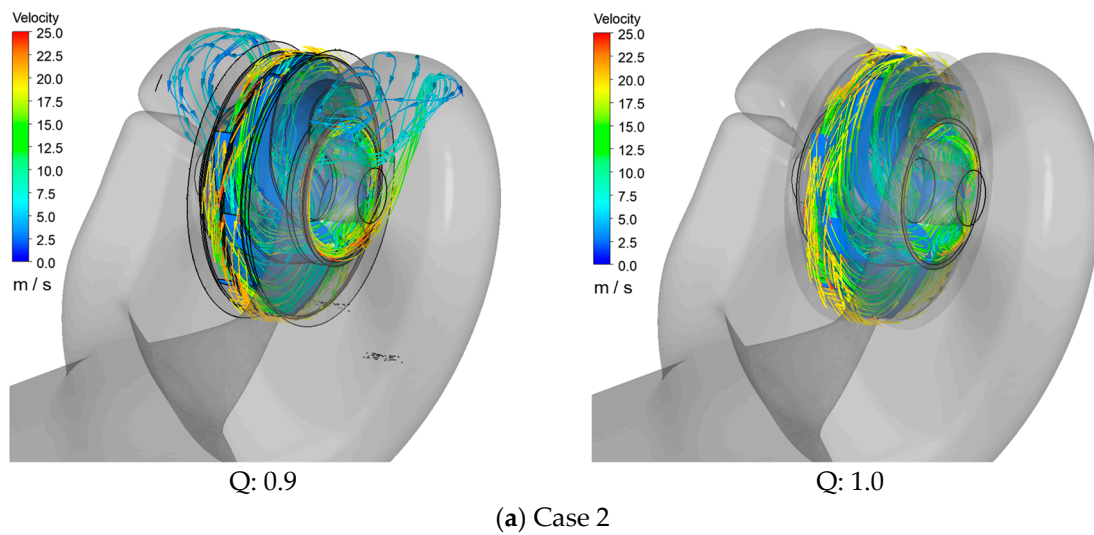


Figure 10. Cont.

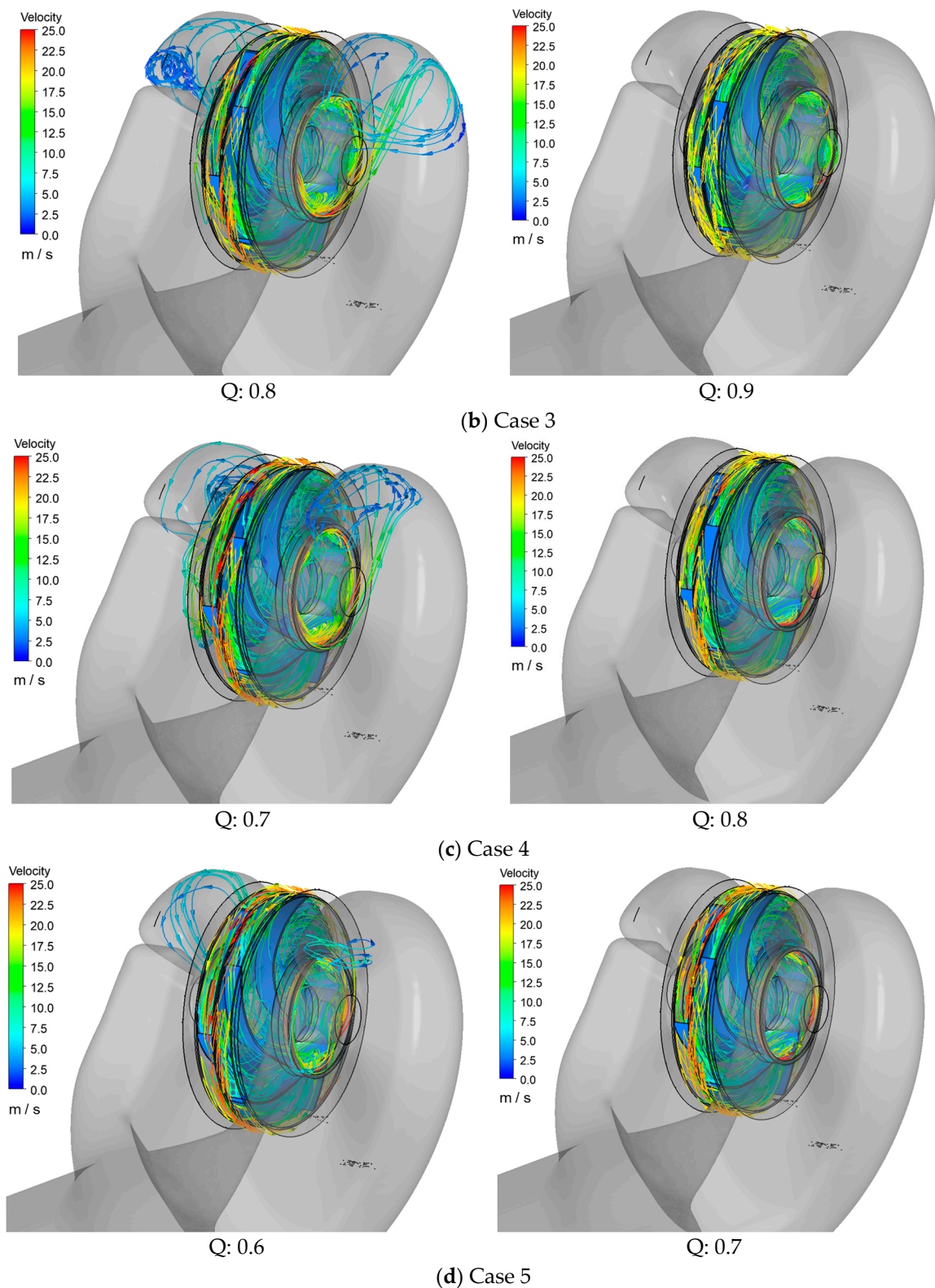


Figure 10. Suction recirculation expressed as a streamline in Cases 2–5.

Figure 11 was acquired using Turbo Mode in ANSYS's CFD-Post. The measurement location is shown in the top-right corner of Figure 9, positioned ahead of the impeller's leading edge (LE) at the 0.2 location in the streamwise direction [42]. The distribution of the velocity streamwise was organized in each case according to the flow rate. At flow point 0.6, all the cases showed a negative flow at the impeller inlet. A negative flow was

observed for flow point 0.7 in Case 5; for flow point 0.8, in Cases 4 and 5; for flow point 0.9, in Cases 3, 4, and 5; and at flow point 1.0, no negative flow was observed in any case. These results align with the findings from Figure 8 to Figure 10, demonstrating that larger shroud diameters lead to backward flow at lower flow rates. In Case 1, where d_{1a} is largest and the d_{1a}/d_{1i} ratio is highest, the negative velocities reach -6 m/s at the 1.0 flow point, and the velocity reaches -11 m/s at the lower flow point 0.6, observed near Span 0.9. Here, Span 0 represents the hub, and Span 1.0 indicates the shroud [42], with Span 0.9 denoting proximity to the shroud. Moreover, in Case 1, the negative flow is even more visible at spans lower than 0.9 as the flow rate decreases, implying that the area of negative flow into the impeller inlet increases at lower flow rates. Also, the velocity of this negative flow increases with a decreasing flow rate, potentially impacting the suction casing at lower flow rates. A positive flow is always observed near the lower span hub area, with the primary flow directed towards the hub at even lower rates.

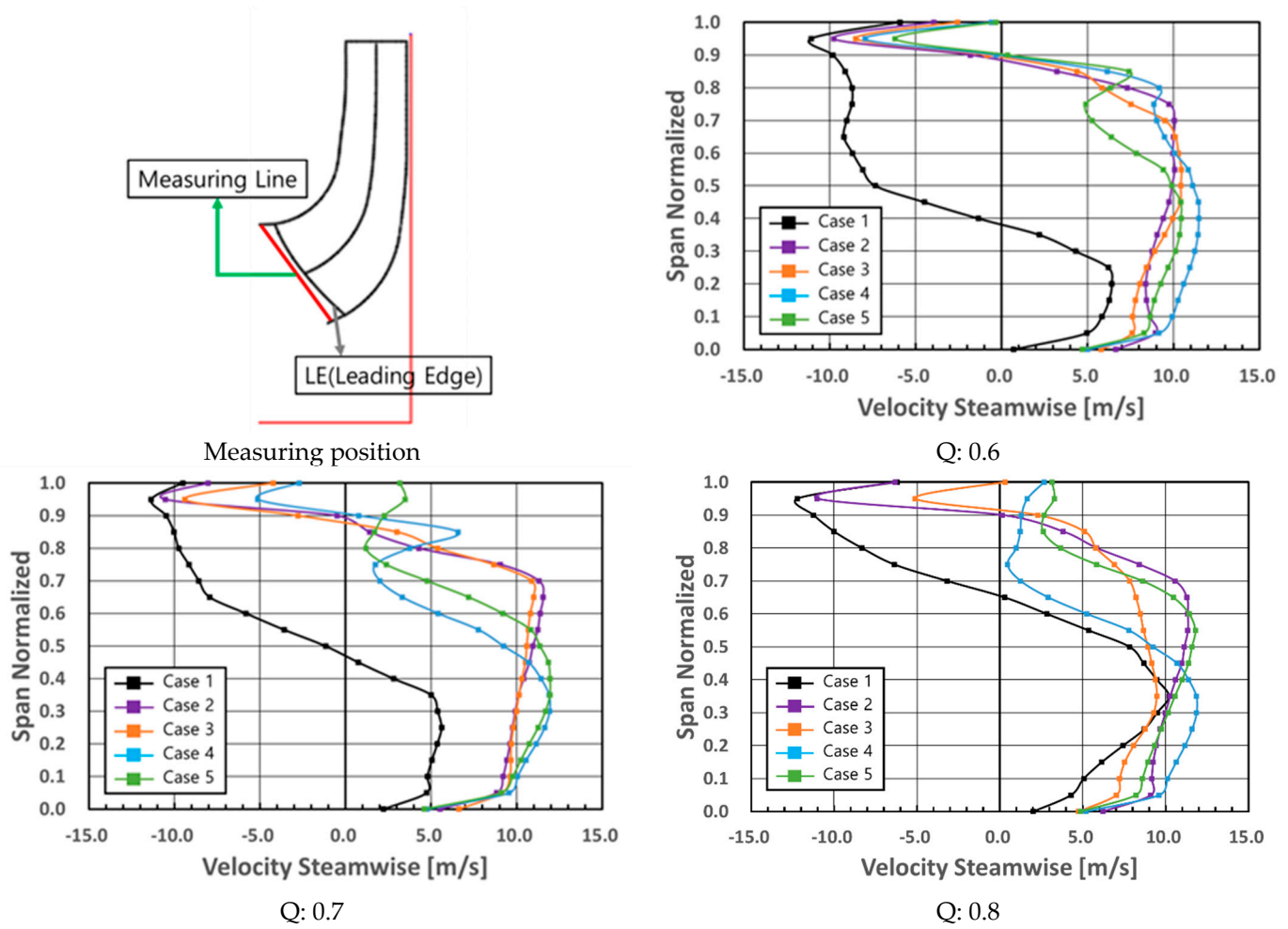


Figure 11. Cont.

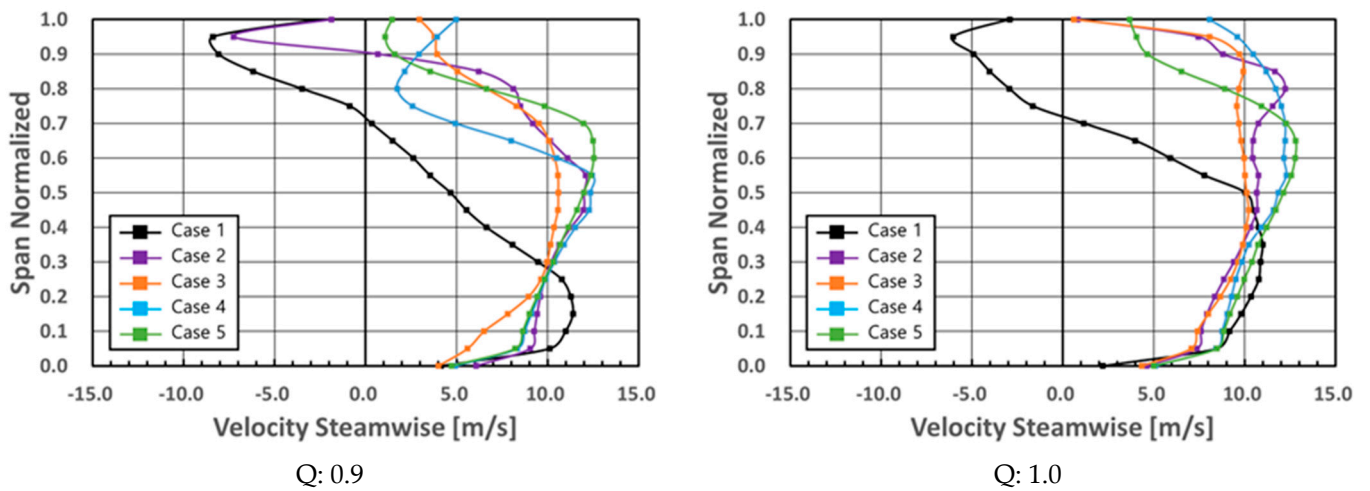


Figure 11. Velocity streamwise distribution near impeller LE in each case according to flow rate.

In the designs of high-flow pumps, the impeller inlet’s diameter is often increased to ensure a cavitation-safe design. However, a larger inlet diameter can make the pump more susceptible to suction recirculation, especially at low flow rates close to the lower limit of the POR (Preferred Operational Range). This suction calculation, which is observed as the flow behavior in the CFD-Post process results, can generate considerable vibration and noise, leading to damaging the pump’s components. Therefore, Figure 12 can serve as an indicator for addressing such issues, showing the flow rate points where suction recirculation occurs based on the ratio of the impeller inlet’s hub to its shroud (d_{1a}/d_{1i}). The blue areas indicate points without recirculation, whereas the red area above the black baseline indicates recirculation.

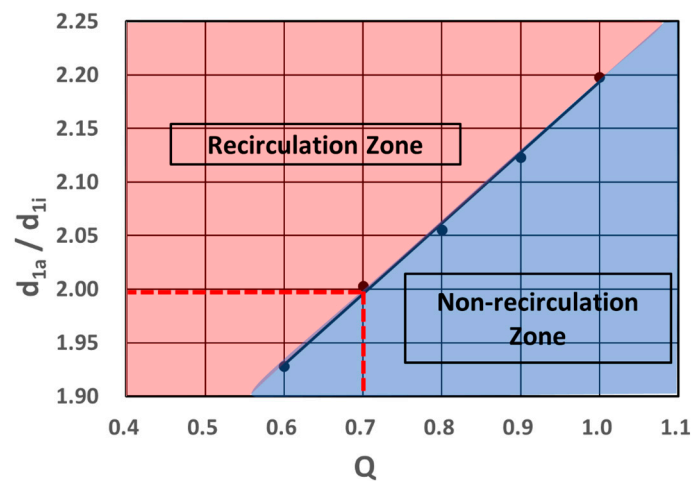


Figure 12. The flow rate at which suction recirculation occurs depending on the diameter ratio (hub-to-shroud ratio) of the impeller inlet.

In BB (between-bearing)-type double-suction pumps, the suction recirculation generated at the impeller inlet can affect the suction casing, making the pump more prone to vibration. Therefore, it is preferable to design to avoid suction recirculation at lower flow rates, mainly closer to 70% of the Best Efficiency Point, as indicated by the lower limit of the POR. As depicted in Figure 12, it is advisable to design a double-suction pump to avoid recirculation occurring below a d_{1a}/d_{1i} ratio of approximately 2.01, where the flow point is 0.7 regarding the lower limit of the POR. Furthermore, the relationship between the impeller inlet’s diameter ratio and the flow rate follows the line $d_{1a}/d_{1i} = 0.6602Q + 1.5334$ within a diameter ratio of 1.93 to 2.20, as this study explored.

5. Conclusions

This study investigated the impact of varying the impeller inlet's geometry size on the performance and stability of double-suction pumps. Five different impeller hub-to-shroud ratios were compared for a range of flow rates while observing the suction recirculation phenomena and evaluating the pump's performance. The CFD simulation method was validated through experiments for a selected impeller design across a range of flow rates by comparing the changes in the head and efficiency before extending the research to different impeller sizes. In the case of the impeller sizes, a larger impeller inlet was observed to have a high head at lower flow rates, resulting in low efficiency, whereas a smaller impeller inlet had high efficiency.

The study also examined the suction recirculation phenomenon at the impeller's inlet. Suction recirculation was mainly observed at flow rates lower than the BEP, where the flow rate was closer to the lower limit of the POR, indicated by 70% of the BEP. These circulations negatively impact the pump's stability and efficiency, potentially leading to issues like vibration and noise. The study found a trend of the suction recirculation phenomenon decreasing as the impeller inlet's hub-to-shroud diameter ratio reduces. In conclusion, the study suggests that the design of the impeller inlet's geometry in double-suction pumps has a high influence on the pump's performance and stability. The flow point where suction recirculation occurs varies according to the hub-to-shroud ratio (d_{1a}/d_{1i}) of the impeller inlet. To avoid suction recirculation for the given double suction pump, especially at the lower limit of the POR (70% flow rate of the BEP), the pump's impeller diameter ratio should be 2.01, and the relationship between the flow point and the impeller inlet's diameter ratio follows the $d_{1a}/d_{1i} = 0.6602Q + 1.5334$ linearity behavior for a range of 1.93 to 2.20 diameter ratios.

Author Contributions: Conceptualization, H.J. and J.S.; Validation, H.J. and J.S.; Formal analysis, H.J.; Writing—original draft, H.J.; Visualization, H.J. and J.S. All authors have read and agreed to the published version of the manuscript.

Funding: This article was supported by “Regional Innovation Strategy (RIS)” through the National Research Foundation of Korea (NRF) funded by the Ministry of Education (MOE) (2021RIS-003).

Data Availability Statement: The original contributions presented in the study are included in the article, further inquiries can be directed to the corresponding author.

Conflicts of Interest: Author Hyunjun Jang was employed by High Turbo Machinery (HTM) Co. The remaining authors declare that the research was conducted in the absence of any commercial or financial relationships that could be construed as a potential conflict of interest.

Nomenclature

Abbreviation	Description
AOR	Allowable Operating Region
BB	Between-Bearing
BEP	Best Efficiency Point
CFD	Computational Fluid Dynamics
LE	Leading Edge
NPSH	Net Positive Suction Head
OH	Overhung
POR	Preferred Operating Region
RANS	Reynolds-Averaged Navier–Stokes
SST	Shear Stress Transport
VPF	Vane-Passing Frequency
Parameter	Description
d_{1a}	Shroud diameter and eye diameter (mm)
d_n	Hub diameter (mm)
f_q	Impeller eyes per impeller: single entry $f_q = 1$; double entry $f_q = 2$

k_n	Blockage caused by hub: $k_n = 1 - d_n^2/d_1^2$
n	Rotational speed (rpm)
Q	Volumetric flow rate, flow (m ³ /h)
Q_E	Flow rate through axial-thrust-balancing device (m ³ /h)
Q_h	Flow rate through auxiliaries (m ³ /h)
Q_{La}	Total flow rate through impeller: $Q_{La} = Q + Q_{sp} + Q_E + Q_h = Q/\eta_v$ (m ³ /h)
Q_{sp}	Leakage flow rate through seal at impeller inlet (m ³ /h)
α_1	Angle between directions of circumferential and absolute velocity, 1: impellerblade's leading edge (°)
β_1	Angle between relative velocity vector and the negative direction of circumferential velocity, 1: impeller blade's leading edge (°)
η_v	Volumetric efficiency (%)
d_2	Impeller's outer diameter [mm]
u_2	Impeller outer diameter tip speed, $u_2 = K_u \sqrt{2gH}$ (m/s)
K_u	The values computed using a Stepanoff chart [34]
H	Head, $H = \frac{P_{Total, outlet} - P_{Total, Inlet}}{\rho g}$ (m)
g	Gravitational acceleration (m/s ²)
ρ	Liquid density (kg/m ³)

References

1. API610; Centrifugal Pumps for Petroleum, Petrochemical and Natural Gas Industries. 6.9 Dynamics, Table 8 Vibration Limits for Overhung and Between-Bearing Pumps. American Petroleum Institute: Washington, DC, USA, 2010.
2. Wu, D.; Ren, Y.; Mou, J.; Gu, Y. Investigation of the correlation between noise & vibration characteristics and unsteady flow in a circulator pump. *J. Mech. Sci. Technol.* **2017**, *31*, 2155–2166.
3. Nelson, W.E. Pump vibrations. In *Proceedings of the 9th International Pump Users Symposium*; Turbomachinery Laboratories, Department of Mechanical Engineering, Texas A&M University: College Station, TX, USA, 1992.
4. Fraser, W.H. Recirculation Centrifugal Pumps. In *Proceedings of the 10th Turbomachinery Symposium*; Turbomachinery Laboratories, Texas A&M University: College Station, TX, USA, 1981; pp. 95–100.
5. Breugelmans, F.A.; Sen, M. Prerotation and Fluid Recirculation in the Suction Pipe of Centrifugal Pumps. In *Proceedings of the 11th Turbomachinery Symposium*; Turbomachinery Laboratories, Texas A&M University: College Station, TX, USA, 1982; pp. 165–180.
6. Ashihara, K.; Goto, A.; Kamijo, K. Improvements of Inducer Inlet Backflow Characteristics Using 3-D Inverse Design Method. In *Proceedings of the 38th AIAA/ASME/SAE/ASEE Joint Propulsion Conference & Exhibit*, Indianapolis, IN, USA, 7–10 July 2002; AIAA: Reston, VA, USA, 2002; p. 4158.
7. Mousmoulis, G.; Karlsen-Davies, N.; Aggidis, G.; Anagnostopoulos, I.; Papantonis, D. Experimental analysis of cavitation in a centrifugal pump using acoustic emission, vibration measurements and flow visualization. *Eur. J. Mech.-B/Fluids* **2019**, *75*, 300–311. [[CrossRef](#)]
8. Nelson, W. Pump vibration analysis for the amateur. In *Proceedings of the 4th International Pump Users Symposium*; Turbomachinery Laboratories, Department of Mechanical Engineering, Texas A&M University: College Station, TX, USA, 1987.
9. Kushwaha, T.N. CW pump fluid induced vibration troubleshooting methodology. *Procedia Eng.* **2016**, *144*, 274–282. [[CrossRef](#)]
10. Yamanishi, N.; Fukao, S.; Qiao, X.; Kato, C.; Tsujimoto, Y. LES Simulation of Backflow Vortex Structure at the Inlet of an Inducer. *ASME J. Fluids Eng.* **2007**, *129*, 587–594. [[CrossRef](#)]
11. Kang, D.; Yonezawa, K.; Ueda, T.; Yamanishi, N.; Kato, C.; Tsujimoto, Y. Large Eddy Simulation of the Dynamic Response of an Inducer to Flow Rate Fluctuations. *Int. J. Fluid Mach. Syst.* **2009**, *2*, 431–438. [[CrossRef](#)]
12. Shim, H.-S.; Kim, K.-Y.; Choi, Y.-S. Three-objective optimization of a centrifugal pump to reduce flow recirculation and cavitation. *J. Fluids Eng.* **2018**, *140*, 091202. [[CrossRef](#)]
13. Capurso, T.; Bergamini, L.; Torresi, M. Design and CFD performance analysis of a novel impeller for double suction centrifugal pumps. *Nucl. Eng. Des.* **2019**, *34*, 155–166. [[CrossRef](#)]
14. Yao, Z.; Wang, F.; Qu, L.; Xiao, R.; He, C.; Wang, M. Experimental investigation of time-frequency characteristics of pressure fluctuations in a double-suction centrifugal pump. *J. Fluids Eng.* **2011**, *133*, 101303. [[CrossRef](#)]
15. Wang, Z.; Qian, Z.; Lu, J.; Wu, P. Effects of flow rate and rotational speed on pressure fluctuations in a double-suction centrifugal pump. *Energy* **2019**, *170*, 212–227. [[CrossRef](#)]
16. Hatano, S.; Kang, D.; Kagawa, S.; Nohmi, M.; Yokota, K. Study of cavitation instabilities in double-suction centrifugal pump. *Int. J. Fluid Mach. Syst.* **2014**, *7*, 94–100. [[CrossRef](#)]
17. Matlakala, M.E.; Kallon, D.V.V.; Mogapi, K.E.; Mabelane, I.M.; Makgopa, D.M. Influence of Impeller Diameter on the Performance of Centrifugal pumps. *IOP Conf. Ser. Mater. Sci. Eng.* **2019**, *655*, 012009. [[CrossRef](#)]

18. Al-Obaidi, A.; Qubian, A. Effect of outlet impeller diameter on performance prediction of centrifugal pump under single-phase and cavitation flow conditions. *Int. J. Nonlinear Sci. Numer. Simul.* **2022**, *23*, 1203–1229. [[CrossRef](#)]
19. Shi, W.; Zhou, L.; Lu, W.; Pei, B.; Lang, T. Numerical prediction and performance experiment in a deep-well centrifugal pump with different impeller outlet width. *Chin. J. Mech. Eng.* **2013**, *26*, 46–52. [[CrossRef](#)]
20. Reddy, S.T.C.; Ramana Murty, G.V.; Prasad, M.V.S.S.S.M.; Reddy, D.N. Experimental studies on the effect of impeller width on centrifugal compressor stage performance with low solidity vaned diffusers. *Proc. Inst. Mech. Eng. Part A J. Power Energy* **2007**, *221*, 519–533. [[CrossRef](#)]
21. Tan, M.G.; Liu, H.L.; Yuan, S.Q.; Wang, Y.; Wang, K. Effects of blade outlet width on flow field and characteristic of centrifugal pumps. In Proceedings of the ASME Fluids Engineering Division Summer Conference, Vail, CO, USA, 2–6 August 2009; pp. 51–60.
22. Zhu, D.; Tao, R.; Xiao, R. Anti-cavitation design of the symmetric leading-edge shape of mixed-flow pump impeller blades. *Symmetry* **2019**, *11*, 46. [[CrossRef](#)]
23. Sano, T.; Iino, M.; Maeda, S. Effect of Leading Edge Profile on Cavitation Performance of Mixed Flow Impeller. *J. Phys. Conf. Ser.* **2021**, *1909*, 012018. [[CrossRef](#)]
24. Balasubramanian, R.; Bradshaw, S.; Sabini, E. Influence of impeller leading edge profiles on cavitation and suction performance. In Proceedings of the Middle East Turbomachinery Symposia—2013 Proceedings, Doha, Qatar, 17–20 March 2013; Turbomachinery Laboratory, Texas A&M Engineering Experiment Station: College Station, TX, USA, 2013.
25. Dönmez, A.H.; Yumurtacı, Z.; Kavurmacıoğlu, L. Influence of Inlet Vane and Wrap Angles on Cavitation Behavior of a Centrifugal Pump. *J. Appl. Fluid Mech.* **2023**, *16*, 519–531.
26. Luo, X.; Zhang, Y.; Peng, J.; Xu, H.; Yu, W. Impeller inlet geometry effect on performance improvement for centrifugal pumps. *J. Mech. Sci. Technol.* **2008**, *22*, 1971–1976. [[CrossRef](#)]
27. Shukla, S.N.; Kshirsagar, J. Numerical prediction of cavitation in model pump. In Proceedings of the ASME International Mechanical Engineering Congress and Exposition, Boston, MA, USA, 31 October–6 November 2008; Volume 48739.
28. Ceyrowsky, T.; Hildebrandt, A.; Schwarze, R. Numerical investigation of the circumferential pressure distortion induced by a centrifugal compressor’s external volute. In Proceedings of the Turbo Expo 2018: Turbomachinery Technical Conference & Exposition, Oslo, Norway, 11–15 June 2018. ASME paper GT2018-75919.
29. Cravero, C.; Marsano, D.; Sishtla, V.; Halbe, C.; Cousins, W.T. Numerical investigations of near surge operating conditions in a two-stage radial compressor with refrigerant gas. *J. Eng. Gas Turbines Power* **2024**, *146*, 021010. [[CrossRef](#)]
30. Li, L.; Xu, W.; Tan, Y.; Yang, Y.; Yang, J.; Tan, D. Fluid-induced vibration evolution mechanism of multiphase free sink vortex and the multi-source vibration sensing method. *Mech. Syst. Signal Process.* **2023**, *189*, 110058. [[CrossRef](#)]
31. Xia, L.; Zou, Z.J.; Wang, Z.H.; Zou, L.; Gao, H. Surrogate model based uncertainty quantification of CFD simulations of the viscous flow around a ship advancing in shallow water. *Ocean Eng.* **2021**, *234*, 109206. [[CrossRef](#)]
32. Cravero, C.; De Domenico, D.; Marsano, D. Uncertainty Quantification Analysis of Exhaust Gas Plume in a Crosswind. *Energies* **2023**, *16*, 3549. [[CrossRef](#)]
33. Gülich, J.F. *Centrifugal Pumps*, 3rd ed.; Springer: Berlin, Germany, 2014; pp. 375–396. ISBN 978-3-642-40114-5.
34. Stepanoff, A.J. *Centrifugal and Axial Flow Pumps. Theory, Design, and Application*; John Wiley & Sons Inc.: New York, NY, USA, 1957.
35. Menter, F.R. Two-equation eddy-viscosity turbulence models for engineering applications. *AIAA J.* **1994**, *32*, 1598–1605. [[CrossRef](#)]
36. Bardina, J.E.P.G.; Huang, P.; Coakley, T.; Bardina, J.; Huang, P.; Coakley, T. Turbulence modeling validation. In Proceedings of the 28th Fluid Dynamics Conference, Snowmass Village, CO, USA, 29 June–2 July 1997; p. 2121.
37. Shim, H.S.; Afzal, A.; Kim, K.Y.; Jeong, H.S. Three-Objective Optimization of a Centrifugal Pump with Double Volute to Minimize Radial Thrust at Off-Design Conditions. *Proc. Inst. Mech. Eng. Part A J. Power Energy* **2016**, *236*, 598–615. [[CrossRef](#)]
38. Wang, Y.; Liu, H.; Yuan, S.; Tan, M.; Shu, M. Applicability of turbulence models on characteristics prediction of centrifugal pumps. In Proceedings of the Fluids Engineering Division Summer Meeting, Reno, NE, USA, 8–11 January 2011; Volume 44403, pp. 1295–1301.
39. Wang, S.; Tan, J.; Yu, Z. Comparison and experimental validation of turbulence models for an axial flow blood pump. *J. Mech. Med. Biol.* **2019**, *19*, 1940063. [[CrossRef](#)]
40. Osman, F.K.; Zhang, J.; Lai, L.; Kwarteng, A.A. Effects of turbulence models on flow characteristics of a vertical fire pump. *J. Appl. Fluid Mech.* **2022**, *15*, 1661–1674.
41. Zhou, L.; Bai, L.; Li, W.; Shi, W.; Wang, C. PIV validation of different turbulence models used for numerical simulation of a centrifugal pump diffuser. *Eng. Comput.* **2018**, *35*, 2–17. [[CrossRef](#)]
42. *ANSYS CFD-Post User Guide*; Release 2021R2; ANSYS Inc.: Canonsburg, PA, USA, 2021; pp. 373–407.

Disclaimer/Publisher’s Note: The statements, opinions and data contained in all publications are solely those of the individual author(s) and contributor(s) and not of MDPI and/or the editor(s). MDPI and/or the editor(s) disclaim responsibility for any injury to people or property resulting from any ideas, methods, instructions or products referred to in the content.